Correlation of structural, magnetic, and electronic transitions of a novel charge-gradient $YBa_2Cu_3O_{\nabla x}$ film

B. J. Taylor,[1,*] C. A. McElroy,[2,3] I. K. Lum,[3,4] A. M. Leese de Escobar,[1] M. C. de Andrade,[1] T. J. Wong,[2] E. Y. Cho,[2] and M. B. Maple[2,3,4]

[1]*Space and Naval Warfare Systems Center–Pacific, Cryogenic Exploitation of RF (CERF) Lab, 53470 Strothe Road, San Diego, California 92152, USA*

[2]*University of California, San Diego, Department of Physics, 9500 Gilman Drive, La Jolla, California 92093-0319, USA*

[3]*Center for Advanced Nanosciences, University of California, San Diego, California 92093, USA*

[4]*Materials Science and Engineering Program, University of California, San Diego, La Jolla, California 92093, USA*

(Received 31 December 2014; revised manuscript received 7 April 2015; published 24 April 2015)

Comprehensive investigations of superconductivity in the charge-doped high-temperature superconducting cuprates often involve examining the evolution of physical properties within a series of samples having controlled variations of some dopant element—most frequently oxygen. Many important observations have been extracted from such experiments, however, the associated measurements are by nature discrete snapshots of the evolving material. We demonstrate here a novel approach to sample preparation of the high-T_c cuprate $YBa_2Cu_3O_x$. By post-annealing a uniformly overdoped $YBa_2Cu_3O_x (x \approx 7.0)$ film in a low pressure O_2 atmosphere with a thermal gradient across the film length, we have successfully grown a charge-gradient $YBa_2Cu_3O_{\nabla x}$ sample, i.e., a film having a varying oxygen doping level along the length of the substrate. Surprisingly, we observe three distinct regimes of oxygen distribution across the sample, as well as behavior pointing to a full alignment within the *a-b* plane.

DOI: 10.1103/PhysRevB.91.144511 PACS number(s): 74.25.Dw, 74.62.Bf, 74.25.Bt

I. INTRODUCTION

The charge doping—temperature, $p - T$, phase diagram of high critical temperature (high-T_c) superconducting cuprates have been extensively studied for over two decades as an accurate understanding of it is an essential step towards establishing the origin of superconductivty in these materials. In many of these compounds the oxygen content, in addition to driving structural transitions, determines the amount of hole or electron doping in the superconducting CuO_2 planes. The standard method for investigating the evolution of electronic ground states in these materials is to prepare a series of samples with various fixed levels of oxygen content upon which to perform experimental investigation of physical properties; see, e.g., Refs. [1–6]. It would, in many cases, be beneficial to have even higher experimental resolution of the evolving properties under investigation—ideally a continuum of physical specimens to examine. Here, we demonstrate a novel method for the growth of a single film having a monotonically varying oxygen content as a function of the physical distance along the sample, resulting in a "phase diagram on a chip" of the high-T_c cuprate $YBa_2Cu_3O_x$, which we refer to as $YBa_2Cu_3O_{\nabla x}$. The film was characterized with bulk magnetization M(T), x-ray diffraction, and resistivity R(T) measurements taken in succession, followed by polarized optical imaging. From these measurements we can confirm the monotonically evolving charge doping distribution along the film. A smooth evolution of oxygen content along the sample length conforming to the local temperature along the thermal gradient is expected. However, contrary to this assumption, we find three physically distinct regimes of oxygen distribution. From analysis of the data we observe (1) a full stabilization of the $p = 1/7$ doping state which depletes a wide range of the adjacent hole concentrations as well as a quasistabilization of the $p = 1/8$ doping state, and (2) behavior consistent with a de-twinning of the lattice of the film.

II. EXPERIMENT

A. Sample preparation

An epitaxial $YBa_2Cu_3O_x$ film was grown on a ⟨001⟩ $SrTiO_3$ substrate ($\ell \times w = 1.0$ cm $\times 0.5$ cm) via the pulsed laser ablation method using a 248-nm laser. Following the method of Ref. [7], the target material used for the ablation process was prepared from stoichiometric quantities of Y_2O_3, $Ba(NO_3)_2$, and CuI. All heating, cooling, and annealing of the target material were carried out under flowing oxygen at a rate of $\sim$150 cm^3/min. During the ablation process, the laser beam was focused onto the target over an area of 1 mm $\times$ 2 mm with an incident energy of $\sim$110 mJ, and a pulse rate of 10 Hz. The film was deposited at 780 °C in 280 mTorr of flowing oxygen with the incoming gas directed into the laser plume directly above the substrate/film. Immediately following the film growth process the oxygen pressure in the chamber was increased to 950 Torr at a rate of $\approx$65–70 Torr/min. The oxygen was flowed into the chamber through an alternate inlet so the gas was not flowing across the sample. Concurrent with the increase in chamber pressure, the film was cooled to 450 °C at a rate of 10 °C/min and annealed at 950 Torr for a period of 16 h. The film undergoes the tetragonal to orthorhombic phase transition [8] at $P \approx 760$ Torr, $T \approx 670$ °C. The pressure/temperature continues to increase/decrease to $P \approx 950$ Torr, $T \approx 645$ °C, and from there the sample is cooled to 450 °C. Under these conditions the O(1) chain-layer (β) site is preferentially occupied with a fractional occupancy of ≈ 0.8 at the beginning of the anneal period, and approaches full occupancy as the sample is finally cooled to room temperature in a fully oxygenated state at rate of 5 °C/min. The oxygen pressure at this temperature was 870 Torr.

*benjamin.taylor4@navy.mil

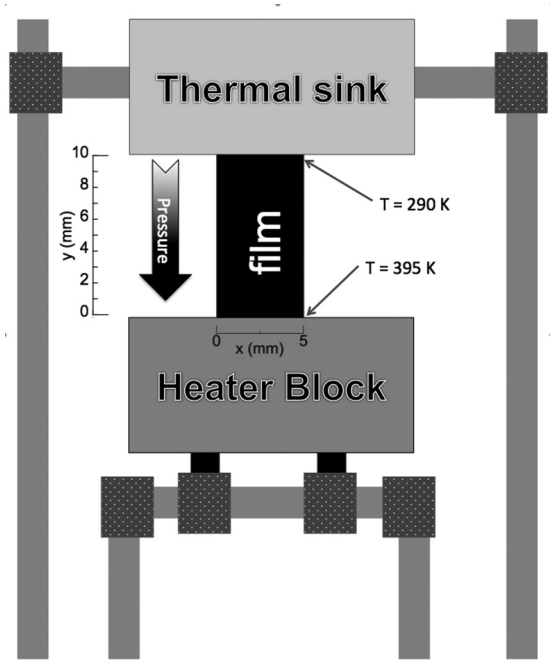

FIG. 1. Schematic of the apparatus used to produce the $YBa_2Cu_3O_{\nabla x}$ film. The y(mm) scale shown corresponds to the sample orientation shown in Fig. 7(b) below.

Following the *in situ* annealing of the deposited film, the sample is initially in the fully overdoped $p \approx 0.20$ state ($YBa_2Cu_3O_7$). The sample is removed from the deposition chamber and placed in an annealing apparatus which applies heat (via a heater block) to one edge of the substrate/film with the opposite edge of the substrate/film in contact with a stainless steel block that is thermally sunk to the chamber walls—resulting in a thermal gradient across the sample as shown in Fig. 1. The apparatus is placed into the deposition chamber which is then evacuated to $P \lesssim 10^{-6}$ Torr and back-filled with oxygen to atmospheric pressure multiple times. The pressure is then reduced to $P \approx 120$ mTorr and the chamber is sealed. The temperature of the heater block is raised to 395 °C at a rate of 5 °C/min while the pressure is monitored to keep it stable. (A sample prepared under conventional annealing conditions with the same temperature and oxygen pressure will result in a uniform doping of $p \approx 0.12$) [9,10]. Following this annealing procedure, the physical properties of the film were examined with bulk magnetization M(T), x-ray diffraction, and resistance R(T) measurements taken successively. Zero field resistance and x-ray data confirm the quality of the film and the x-ray data confirms a c-axis orientation.

After performing magnetization and x-ray measurements on the prepared film of $YBa_2Cu_3O_{\nabla x}$, the film was chemically etched for 1 min in a nonaqueous solution of 1% bromine in methanol as per Ref. [11]. The bromine etch has been previously used to improve the reproducibility of tunnel junction fabrication [12]. The electrode materials were then deposited through dc magnetron sputtering first with 10 nm of Ti followed by 200 nm of Au. Resistance bridges aligned along the sample width (parallel to constant concentrations of oxygen within the $YBa_2Cu_3O_x$ lattice) were then photolithographically patterned using a hard baked mask consisting of NR9-3000PY negative photoresist. The Au-Ti layer was etched in unmasked areas through a Transcene KI/I2 etch (<2 min) followed by a short (<1 min) etch in 49% hydrofluoric acid to remove the Ti sticking layer. The $YBa_2Cu_3O_x$ film was subsequently removed using 8% phosphoric acid for about 1 min. After stripping the bridge photomask, an additional photolithographic process was performed using Shipley 1813 photoresist to mask the electrical contacts for a final KI/I2 gold etch to remove the metallic short on the resistance bridge. The final sample dimensions for each line are $\ell \times w \times t = 0.25019$ cm $\times$ 0.01143 cm $\times$ 1300 nm. Gold wires (0.002-inch diameter) were attached to the sample using indium contacts adhered to the gold pads. Polarized optical imaging of the film bridges show no twin structures at the $\sim$10-μm scale.

B. Magnetization

The strength and position of the bulk magnetic response of the $YBa_2Cu_3O_{\nabla x}$ film was measured as follows. A measurement of the magnetization vs temperature $M(T)$ was performed on the sample in a Quantum Design MPMS SQUID magnetometer. Magnetization data were taken with the film length aligned parallel to the applied magnetic field ($H \parallel a$ axis; see Analysis below). The sample was centered at $T = 200$ K in an applied magnetic field of $H = 1$ kOe using a 4-cm scan length (from which it follows that the center position is 2 cm). The sample was mounted such that the high (low) oxygen content edge corresponds to the scan length position of 2.5 cm (1.5 cm). After centering the sample, the magnetic field was reduced to zero and the sample was cooled to $T = 95$ K. Subsequently, a small field of $H = 10$ Oe was applied, and the sample was slowly cooled through the superconducting transition down to $T = 35$ K. For these measurements the autocentering option was disabled so that the center location of the measured signal from the sample can be tracked as a function of temperature. The temperature control was in "No Overshoot" mode. A small upward temperature drift is observed from the recorded beginning and end temperatures of each scan, typically of $\Delta T \approx 0.05$ K.

Given that the oxygen content varies along the film, it is important to recall that as the sample cools, various portions of the film become superconducting when the local critical superconducting temperature T_c is reached. Hence, the magnetization data are essentially a composite of multiple samples at positions y(mm) along the substrate length so that the curve observed is both a measure of $T_c(p)$ and the increase in the diamagnetic response as the sample continues to cool, i.e., $M(T) = \sum_p M(T, p(y))$.

We show in Fig. 2 the induced voltage signal response as detected by the SQUID magnetometer from which the magnetic moment is calculated. A sudden shift of the center of the voltage signal from 2.0 cm to $\sim$2.49 cm is observed as a portion of the sample cools into the superconducting state. As the sample continues to cool, the center of the signal proceeds to move back towards the initial centering position of 2 cm. The center position indicated by the arrows in Fig. 2 is shown as open circle symbols in Fig. 3(b).

Various features in the $M(T)$ data and SQUID magnetic moment center indicated in Figs. 3(a) and 3(b) can be correlated with specific charge doping values of p and features

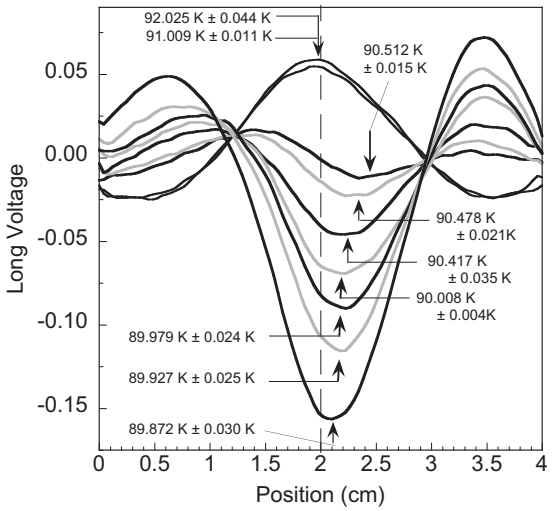

FIG. 2. Voltage signal response of the SQUID magnetometer for the longitudinal magnetic moment of the $YBa_2Cu_3O_{\nabla x}$ sample at temperatures in the vicinity of the superconducting transition. The values of the temperature shown are the mean of the beginning and end temperature recorded by the MPMS for each scan. The error value indicates the range of the temperature during the scan. The arrows indicate the center position of the voltage response as determined by a curve fit. These positions are shown as open circle symbols in Fig. 3(b).

in the $T_c - x$ phase diagram, as determined in Ref. [9], where the dependence of structural properties, hole doping, and the value of T_c upon the oxygen content in a series of high quality single crystals of $YBa_2Cu_3O_x$ were precisely mapped out.

The magnetic moment center feature at $T \approx 87.5$ K [along with the $M(T \approx 86.5$ K) kink] is most likely due to encountering the end of the overdoped region (see Appendix A). Below this, at $T \approx 81$ K, a significant jump (a factor of 7) is observed in the magnitude of the measured magnetic moment along with an approximately 2-mm shift in the center position of the SQUID voltage signal. Taking into account the ~ 3 K difference between the maximum value of T_c of our film and that of the single crystals [9], a value of $T_c \approx 81$ K for the film corresponds to a superconducting transition for a sample having a value of $p \approx 0.141$. For temperatures above $T \approx 81$ K, the $M(T)$ data exhibits a generally positive curvature, however, in the range 68 K $\lesssim T \lesssim$ 81 K, the $M(T)$ data have a linear temperature dependence, as does the center position of the SQUID voltage signal. The value of $T_c = 68$ K for our film corresponds [9] to a hole doping value of $p \approx 0.126$.

Below $T \approx 68$ K, the $M(T)$ data resumes a positive curvature to the lowest temperature measured, and a corresponding kink is seen in the center position as also following a nonlinear temperature dependence. As discussed further below in the context of x-ray diffraction and resistivity measurements, the discontinuity in $M(T)$ and the center signal position is attributable to the film having a wide section with a nearly uniform doping value of $p \approx 1/7$, wherein the adjacent doping states in the interval $(1/8 + \delta) \leqslant p \leqslant (1/6 - \delta)$, $(\delta \approx 0.005)$ are depleted.

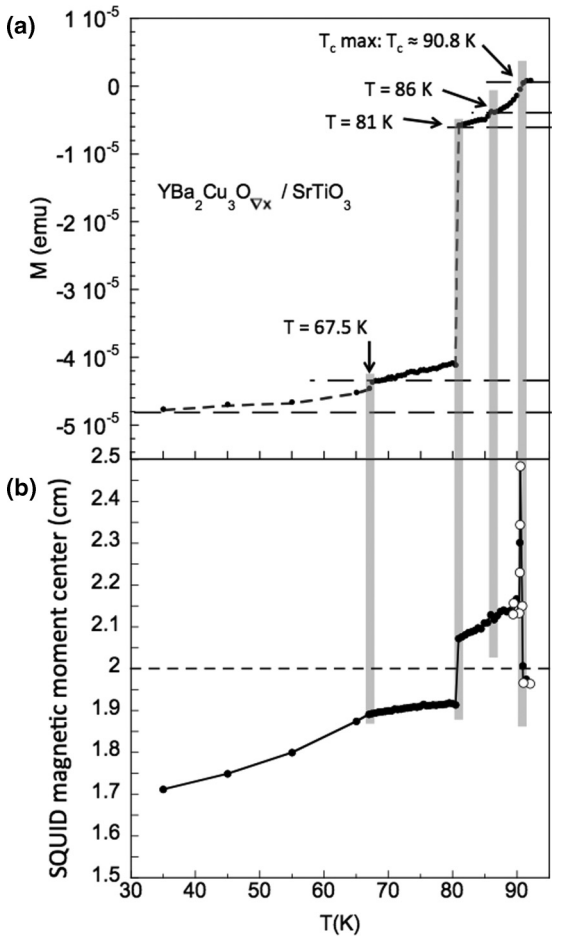

FIG. 3. Magnetization data for the $YBa_2Cu_3O_{\nabla x}$ film. (a) Total magnetic moment vs temperature $M(T)$ of the $YBa_2Cu_3O_{\nabla x}$ sample. (b) Magnetic moment signal center in the SQUID magnetometer vs temperature, $M_{\text{center}}(T)$. Open circles indicate data from voltage signal curves shown in Fig. 2. Filled circles are the average of four magnetization/center position measurements taken at each temperature. The values of 1.5 cm, 2.0 cm, and 2.5 cm of the signal position corresponds to the sample length positions of $y = 0$ mm, $y = 5$ mm, and $y = 10$ mm, respectively. (See also Fig. 7.)

C. X-ray diffraction

Following the taking of the magnetization data, the sample was x-rayed at various positions along the sample length as indicated in Fig. 4 in a Bruker D8 DISCOVER with a two-dimensional (2D) detector and a focused beam spot of $d \approx 350\,\mu$m. X-ray data were taken uniformly along the direction of the applied thermal gradient so as to determine the local oxygen content through the changes in the 2θ positions of the $\langle 00\,\ell \rangle$ reflections. From the $\langle 004 \rangle$ and the $\langle 00\,10 \rangle$ peak locations (see Fig. 4 and Figs. 11 and 12 of Appendix B) the c-axis lattice parameter along the film sample length was determined from the 2θ values extracted from fits to the x-ray data. The hole doping level p of the film was inferred from Eq. (2) of Ref. [9]. The value of the c-axis lattice parameter c(nm) and corresponding values of p as a function of position y(mm) along the sample length are shown in Fig. 5 and also given in Table I. Three distinct physical regions are observed. In the regions from $y \approx$ 0.5–3.0 mm and $y \approx$

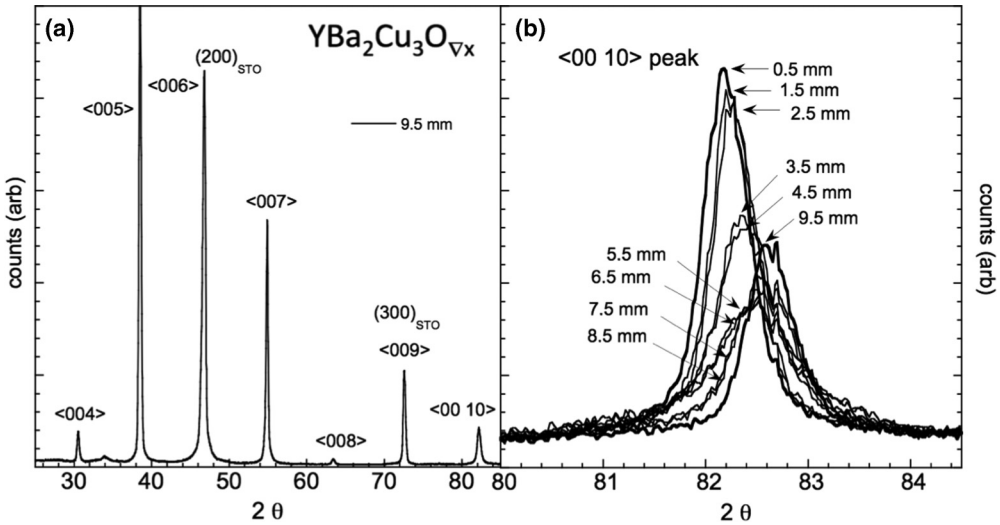

FIG. 4. Integrated x-ray diffraction data for the $YBa_2Cu_3O_{\nabla x}$ film. (a) Full diffraction scan centered at position of $(x,y) =$ (1.67 mm,9.5 mm). See Figs. 1 and 7 for corresponding axis configuration. (b) ⟨00 10⟩ diffraction peak from a series of full diffraction scans at $(x,y) =$ (1.67 mm, [0.5,1.5, . . . 9.5] mm). (See also Figs. 11 and 12 of Appendix B.)

5.0–9.5 mm the change in c(nm) per sample length y(mm) is linearly dependent, with slightly differing slopes. However, in the intermediate region, near $p = 1/7$, c(nm) exhibits little change, implying a wide region of uniform charge doping and then, necessarily, the presence of two highly strained boundaries within the film with a corresponding discontinuity in the oxygen (charge) doping gradient, ∇x (∇p).

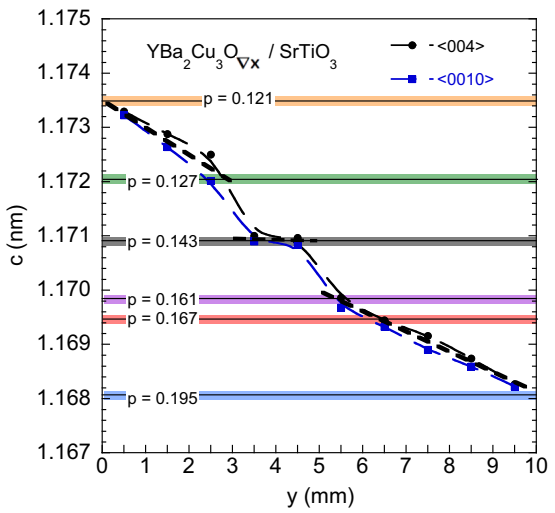

FIG. 5. (Color online) $YBa_2Cu_3O_{\nabla x}$ film c-axis lattice parameter vs position, c(nm) vs y(mm) along the direction of the thermal gradient. Values of c(nm) are calculated from the series of the ⟨004⟩ and ⟨00 10⟩ peaks. Linear fits to the average of the c-axis length determined from the two sets of peaks are shown for three distinct regions. In the regions from $y \approx 0.5$–3.0 mm and $y \approx 5.0$–10 mm the change in hole concentration per sample length is $\Delta p/\Delta y \approx 6.1 \times 10^{-3}$ (holes/Cu)/mm and 7.4×10^{-3} (holes/Cu)/mm, respectively. The intermediate region, in the $p \approx 1/7$ plateau, $\Delta p/\Delta y \approx 7.4 \times 10^{-4}$ (holes/Cu)/mm.

D. Resistivity

After performing magnetization and x-ray measurements on the $YBa_2Cu_3O_{\nabla x}$ film it was prepared for zero field resistance R(T) measurements by lithographic etching. In order to ensure that the $\rho(T)$ measurements sampled a uniform region of oxygen doping/hole content p a single wire was attached to each end of the sample, rather than a standard four-wire measurement. Each wire was soldered to the sample puck at the $V^{\pm}$ and then the $I^{\pm}$ terminals to form a quasi-four-wire resistivity configuration. This results in a short segment of gold in series with the sample segment. The normalized R(T) data is shown in Fig. 6 and in the inset. Values of T_c as a function of y(mm) were determined from the midpoint of the resistive superconducting transition for each position measured. A small nonzero offset can be seen for some of the normalized R(T) data. The resistivity bridge located at $y = 6.39$ mm was not measured as a good electrical contact to the sample was not obtained.

Of particular interest, as shown in Fig. 7(c), is an observed doping dependent difference $\Delta T_c(p)$ between the superconducting transition of the films with respect to that of single crystals *having the same c-axis length* as determined in Ref. [9] (see also Fig. 13 of Appendix C). We note that the values of T_c of the single crystals used in Ref. [9] were determined by measuring the in-field cooling magnetization at 1 Oe (applied parallel to the c axis), with T_c being chosen as the midpoint of the transition. The value of T_c for the film segments was determined from the midpoint of the resistive transition. There is typically a small discrepancy between the values of T_c obtained by the two criteria used, however, such a discrepancy is expected to be systematic as the resistive transition for the film segments is narrow and only broadens by a few degrees for highly underdoped segments. As we discuss further below, the manner in which $\Delta T_c(p)$ evolves is remarkably comparable to the *effects* of in-plane strain on $T_c(p)$ of un-twinned single crystals [13,14] throughout the majority of

TABLE I. c-axis length c(nm) calculated from x-ray data, inferred hole doping content p using Eq. (2) of Ref. [9], and corresponding T_c(K) value of a single crystal (Ref. [9]), and T_c determined from ρ(T) measurements (defined as the midpoint of the resistive transition), as a function of position y along the sample length.

y(mm)	c(nm)$_{\langle 004\rangle}$	p(h/Cu)$_{\langle 004\rangle}$	c(nm)$_{\langle 0010\rangle}$	p(h/Cu)$_{\langle 0010\rangle}$	c(nm)$_{[\mathrm{avg}]}$	p(h/Cu)$_{[\mathrm{avg}]}$	T_c(K)$_{[\mathrm{avg}]}$ Ref. [9]	T_c(K) [ρ(T)]
9.5	1.168267	0.1911	1.168225	0.1920	1.168246	0.1915	89.99	
9.06								89.44
8.5	1.168743	0.1809	1.168593	0.1840	1.168668	0.1825	92.64	
8.17								90.25
7.5	1.169157	0.1727	1.168903	0.1777	1.169030	0.1752	93.72	
7.28								90.5
6.5	1.169448	0.1673	1.169329	0.1694	1.169388	0.1683	93.69	
6.39								–
5.5	1.169863	0.1599	1.169678	0.1631	1.169770	0.1615	92.46	
5.49								81.8
4.61								71.3
4.5	1.170963	0.1424	1.170845	0.1442	1.170904	0.1433	81.57	
3.73								65.9
3.5	1.171005	0.1418	1.170903	0.1433	1.170954	0.1425	80.84	
2.84								64.1
2.5	1.172505	0.1216	1.172015	0.1278	1.172260	0.1247	65.90	
1.96								61.2
1.5	1.172880	0.1170	1.172640	0.1199	1.172760	0.1184	63.73	
1.04								57.2
0.5	1.173300	0.1120	1.173227	0.1129	1.173262	0.1124	61.55	

the film—with the highly strained boundary regions about the $p \approx 1/7$ section deviating from the overall trend. Furthermore, the normalized resistance shows behavior consistent with the *effects* of the sample being under compressive strain [15,16] wherein a systematic reduction of resistance is observed in the underdoped regime relative to the optimally/overdoped segments.

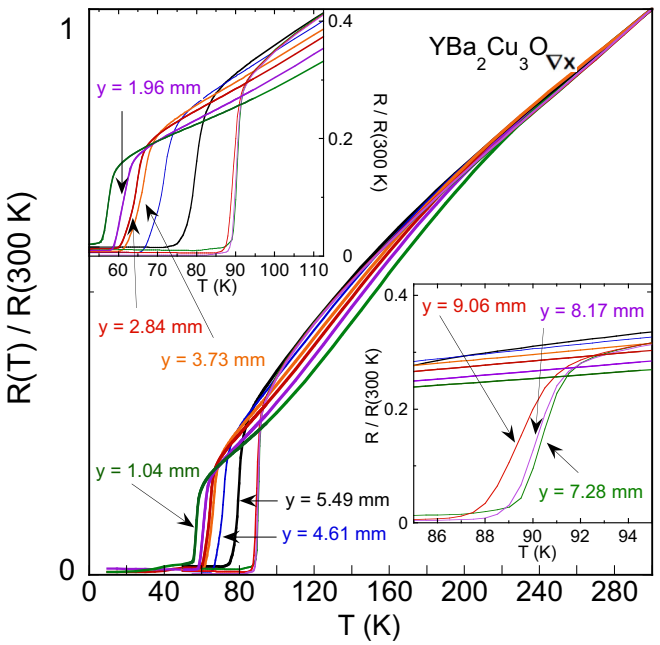

FIG. 6. (Color online) Normalized resistance vs temperature, R(T)/R($T = 300$ K), as a function of sample position.

III. ANALYSIS

Central to understanding the results presented here are the issues of the mechanism of oxygen diffusion within $YBa_2Cu_3O_x$ under normal conditions [17], oxygen ordering in the Cu-O chain layer [18–20], the impact of oxygen ordering effects within $YBa_2Cu_3O_x$ on charge redistribution [14,21–28] and/or changes in interatomic distances [29–32] within the lattice caused by applied strain, pressure, and/or electrostatic bond strain [33–35] and, anisotropic strain sensitivity of T_c [14,21–23,36]. A large part of our analysis below centers on the correlation of the values of p to oxygen ordering, annealing conditions, and stabilization of predicted Cu-O chain states. As described above, the values of p were extracted from the x-ray data via the relationship of the c-axis lattice parameter to p, as determined in Ref. [9] for *unstrained* single crystals. The analysis below shows that our sample exhibits shifts in the value of T_c consistent with the *effects* of *in-plane strain*. As such, we first address the question of strain (pressure) induced charge transfer from the Cu-O chains to the CuO_2 planes. Models which assume an induced charge transfer process have been shown to describe well the hydrostatic pressure dependence of dT_c/dp and that of dT_c/dp_c of single crystals, as well as photoassisted changes of T_c of various $RBa_2Cu_3O_{6+x}$ materials [14,24–28]. However, as noted often, the *in-plane* pressure effects on T_c cannot be described by a simple charge transfer effect within these models [14,21,27]. Additionally, evidence exists that there is no appreciable transfer of charge from the Cu-O chains to the CuO_2 planes for strain along the a, b, and c axes, and rather there is charge redistribution within the CuO_2 layers [22,23] as well as significant changes in the distance of the apical oxygen to the planar copper atom which appears to play a key role in the modulation of the pairing interaction in the

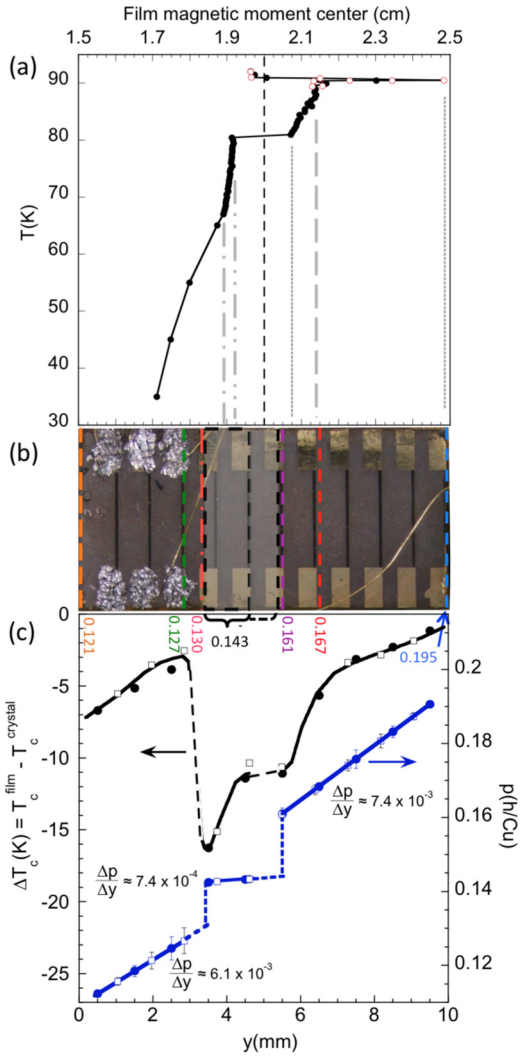

FIG. 7. (Color online) (a) Center of the longitudinal magnetic moment of the $YBa_2Cu_3O_{\nabla x}$ sample with respect to the sample position y(mm). The $M(T)$ scan of sample was taken prior to lithographic etching. (b) $YBa_2Cu_3O_{\nabla x}$ sample after it has been patterned for R(T) measurements. The colored regions indicate values of hole doping inferred from the x-ray data using the relationship the c-axis length and p established in Ref. [9] with the same coloring scheme used in Fig. 5. Note the gray shaded region in the interval 3.4 mm $\lesssim y \lesssim$ 5.6 mm with $p = 0.143 \approx 1/7$. The solid black bracket indicates the region determined from x-ray and R(T) measurements. The dashed extension of the bracket is inferred from $M(T)$ data. The orange dashed line with $p = 0.130$ indicates the inferred doping by linearly extending the $p(y)$ dependence of the highly underdoped region. (c) ΔT_c vs sample position y(mm), and hole concentration vs sample position p vs y(mm). The values of p shown as closed blue circles are determined from the linear fitted mean values of c(nm) shown in Fig. 5 (heavy dashed line). The values of p shown as open blue circles are inferred by correlating the position y of the resistance paths shown in Fig. 6 with an interpolation of closed blue circle p data points. See main text for further details.

CuO_2 plane [29–32]. If though, we were to assume that charge transfer was in fact taking place, then, from Fig. 4 in Ref. [15] we have $d\Delta n_h/dP \approx 22 \times 10^{-3}$ h/GPa at an oxygen content of $x \approx 6.8$ (for hydrostatic applied pressure). Next, by taking values of the c-axis lattice parameter from Fig. 5 (and Table I below), and assuming that the boundary between the $p \approx 1/6$ to 1/7 and 1/7 to 1/8 are abrupt on the scale of a single unit cell, we find an upper bound of the c-axis strain of the order of 0.1 %, which roughly corresponds to a pressure of 90 MPa [22]. From this we find $\Delta n_h \approx +5.5 \times 10^{-3}$, which results in a value of $\Delta T_c \approx +3.7$ K (at the $p \approx 1/7$ to 1/8 boundary), which is 4–5 times smaller and *opposite* to what is observed. Strain values in the uniform regions above and below these boundaries (along the c axis) are $\approx$0.06%/mm–0.08%/mm giving negligible c-axis strain from one unit cell to the next and subsequently no significant transfer of charge or discernible impact on the values of T_c.

Thus, in light of the above considerations, we have a high confidence in the values of p determined above (to within the error bars) via the method of Ref. [9]. Of particular interest are recent studies involving similarly structured compounds that have shown how internal electrostatic fields can produce very large bond strains, subsequently altering dramatically the materials electronic properties [33–35]. We return to the subjects of the role of the apical oxygen and that of electrostatic effects later in the analysis further below.

Taken together, the data show a clear demonstration of the growth of a novel "charge-gradient" $YBa_2Cu_3O_{\nabla x}$ film, with compelling evidence for the existence of a large stabilized region of the highly structurally ordered $p \approx 1/7$ state. We make the case below that (1) reasonable evidence exists supporting a conclusion that the film is likely free of twin structures, and (2) there likely exists an internal electric field which may play both a role in the observed trends of the suppression of the values of $T_c(p)$ and the stability of the structures within the Cu-O chain layer.

As seen in Fig. 7, the sudden jump of the magnitude of $M(T)$ and of the position of $M_{\text{center}}(T)$ at $T = 81$ K is correlated with the observation of a wide region of the film having a nearly uniform oxygen content such that $p \approx 1/7$ as determined from x-ray data. This strongly indicates that the oxygen ordering structure associated with the $p \approx 1/7$ doping level is inherently stable, drawing in the adjacent oxygen that would have supported electronic states corresponding to the doping range $0.130 \lesssim p \lesssim 0.161$. In a related observation, additional features of significance are seen in Fig. 7(c): (1) the *linear* distribution of charge doping in the upper and lower doping regions, (2) the slopes of these regions are such that they don't intersect on the sample length, i.e., a discontinuity in charge doping along the sample is inevitable, and (3) the difference in the critical temperature between the resistively determined value and that calculated for a single crystal from the c-axis length via Ref. [9]. In Fig. 7, the error bars shown represent values of p determined from the c(nm) data of the $\langle 004 \rangle$ and $\langle 00\,10 \rangle$ peaks separately. Values of p were calculated from a curve fit [37] to data shown in Ref. [9]. Closed and open black circles indicating the values of ΔT_c correspond to the closed and open blue circles. See also Fig. 8 for the corresponding oxygen distribution along the sample length. Above $p \approx 1/6$ (O $\approx$ 6.89) the level of oxygen distribution follows the expected evolution given the annealing oxygen pressure and a linear thermal gradient. The $p \approx 1/7$ plateau necessarily deviates from expected distribution. However, we find that the $p \lesssim 1/8$ (O $\lesssim$ 6.72) region *also deviates* from the

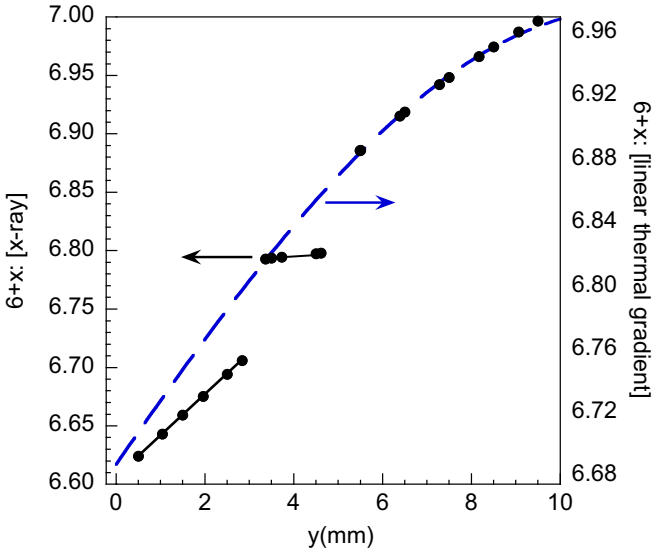

FIG. 8. (Color online) Oxygen content vs sample position, $6+x$ vs y(mm), for the $YBa_2Cu_3O_{\nabla x}$ film as determined from x-ray diffraction and resistivity data and calculated based upon an assumed linear temperature gradient. Solid black circles are calculated from a curve fit [37] to the data shown in Fig. 4(a) of Ref. [9] and from the $p_{[avg]}(y)$ data given in Table I below. The blue dashed line is calculated by assuming a linear temperature profile along the sample (see Fig. 1) and from an empirical fit (via an extrapolation) to the data given in Table I of Ref. [10] with $\log p^*_{O2} = -4.0$ to the expression $6 + x = 5.9867 + 0.88451\exp(-2.0319(1 - T/(275))^2) + 0.1\cosh(1 - T/380)$. The blue dashed line is then arrived at with $T(y) = 395 - 105y$[cm], assuming an equilibrium linear thermal profile [39]. Note that the scales on the left and right y axes are different, and thus there is a small discrepancy between the ranges of oxygen concentration in the film calculated by the two methods. Also, our sample was annealed in an oxygen atmosphere with $P = 120$ mtorr, corresponding to $\log p^*_{O2} = -3.8$, hence a small underestimation of the oxygen content can be expected. However, qualitatively, the two calculations of the oxygen distribution are in good agreement above $y = 5.5$ mm prior to the $p \approx 1/7$ (O ≈ 6.8) discontinuity. Interestingly, the (scaled) blue dashed line intercepts the edge of the $p = 1/7$ plateau and the tail of the $p \lesssim 1/8$ region at the edge of the sample.

expected oxygen distribution, indicating that this region has *also* stabilized its oxygen configuration in a manner contrary to the established relationship between oxygen content and the annealing conditions of oxygen partial pressure and temperature in thermally uniform $YBa_2Cu_3O_x$ bulk, single crystal, and film samples [9,10].

Within the oxygen ordering model for $YBa_2Cu_3O_z$ of Refs. [18–20], ordering within the Cu-O chain layer is described through a branching algorithm wherein the Ortho I ($c = 0.50$) and Ortho II ($c = 0.25$), ($z = 2c + 6$), structures are the generating structures for those of successive levels. The notation $\langle 1 \rangle$ and $\langle 10 \rangle$ denote the Ortho I and Ortho II chain states where a one or zero indicates a completely full or empty Cu-O chain, respectively, and an exponent denotes a repeated structure. The Ortho III structure, $\langle 110 \rangle$, arises from the Ortho I and II structures, i.e., $\langle 1 \rangle + \langle 10 \rangle \rightarrow \langle 110 \rangle$, and so forth. Comparing the hole doping vs oxygen content, p vs $6 + x$, data shown in Fig. 4(a) of Ref. [9] with the branching algorithm

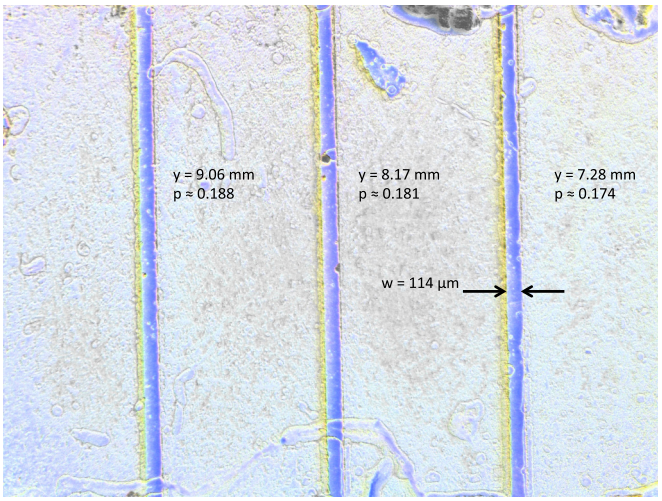

FIG. 9. (Color online) Polarized optical image of the resistivity bridges on the $YBa_2Cu_3O_{\nabla x}$ film. The image shows segments of the film on the overdoped region of the film with $p \approx 0.188$, 0.181, and 0.174. No twinning is observed at the microscale. Thermal grease can be seen remaining on the film and substrate surfaces. Remnant un-etched portions of the film can also be seen.

dependence on the parameter c, the $p = 1/7$ doping state corresponds to the $\langle 1^40 \rangle$ fully ordered chain state ($c = 0.40$) [37]. This result is consistent with our interpretation of the data here as indicative of the $p = 1/7$ state as being exceptionally stable. Similarly, the $p = 1/8 : \langle 1^30110 \rangle$ ($c = 0.36$) state appears to have exerted a stabilizing force on the adjacent (further underdoped) region, albeit in a less dramatic manner, yet still impacting the ordering of the oxygen over a large region. It may be that, under somewhat different annealing conditions, or, given a longer annealing time, the $p = 1/8$ may fully stabilize in the same manner observed for the $p = 1/7$ state.

Evidence for the film being twin-free comes from the absence of detection of twin domains by polarized optical imaging and from the suppression of T_c as a function of hole doping p. Shown in Fig. 9 is a polarized optical image of the overdoped portion of the $YBa_2Cu_3O_{\nabla x}$ film after it has been patterned and measured for ρ(T) properties in zero applied magnetic field. While the limited resolution of optical imaging means we cannot rule out twinning at scales below the microscale [38], the evolution of $\Delta T_c \equiv (T_c[\text{film}] - T_c[\text{singlecrystal}])$ with p does indirectly support this conclusion. As shown in Fig. 10, ΔT_c vs p is remarkably similar to that of dT_c/dp_{ab} vs p for single crystals of $YBa_2Cu_3O_x$ under an (inferred) applied compressive in-plane (a-b) pressure, particularly for values of $p \lesssim 0.130$ where both sets of data are linear. The key differences however, are that $\Delta(dT_c/dp_{ab})/\Delta p < 0$, while $\Delta T_c/\Delta p > 0$, and $(dT_c/dp_{ab}) > 0$ while $\Delta T_c < 0$. The behavior of ΔT_c vs p suggests that the film is behaving as if it were under a strain having primarily in-plane components. Such a strain would be independent of that attributable to the interface with the substrate—which should relax within 70 nm from the interface [40–42] and not affect the remaining 95% of the film volume. If the film were twinned and somehow subject to an in-plane (compressive) strain then both the a axis and b axis of the film are subject to the same force and ΔT_c vs

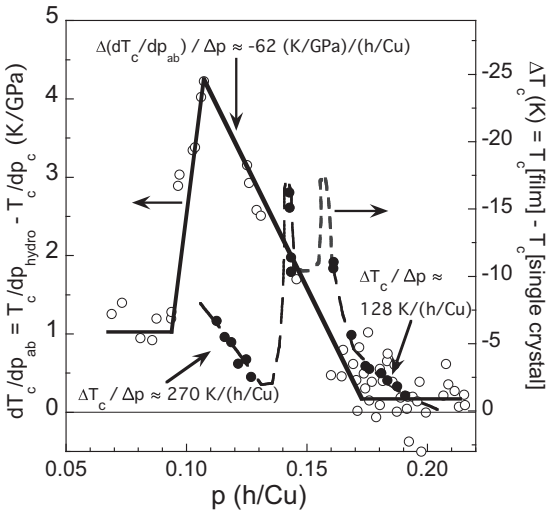

FIG. 10. Comparison of the charge doping dependence of the change of T_c for single crystals due to in–plane pressure to the difference between the values of T_c of the $YBa_2Cu_3O_{\nabla x}$ film and unstrained single crystals. The dT_c/dp_{ab} vs p data (open circles) are deduced values for compressive in-plane (a-b) pressure applied to single crystals of $YBa_2Cu_3O_x$. The single crystal data, along with the linear guide lines, are reproduced from Ref. [14]. Values of ΔT_c vs p (closed circles) for the strained $YBa_2Cu_3O_{\nabla x}$ film are determined from Fig. 13 in Appendix C. The short dashed line is speculative as to the strain effects at the boundary between the $p \approx 1/7$ and $p \approx 1/6$ regions. Note the sign reversal used for the (right) ΔT_c axis. A negative impact on T_c is consistent with compressive/expansive strain along the a/b-axis direction.

p can reasonably be expected to follow dT_c/dp_{ab} vs p. In contrast, if the sample is twin-free, in order to have $\Delta T_c < 0$, the sample must have a strain imbalance between the a axis and b axis directions such that there is a greater compression along the a axis, a greater expansion along the b axis, or compression along the a axis along with expansion along the b axis [14,22]. The linearity of $\Delta T_c(p)$ (for $p \lesssim 0.130$ and $p \gtrsim 0.175$) is consistent with *the effects of* uniform strain in the two sections of the film excluding the boundaries of, and within, the $p \approx 1/7$ region.

The as-grown sample here is almost certainly twinned, even after *in situ* annealing in a high pressure oxygen atmosphere. However, the sample (single crystal $SrTiO_3$ substrate and $YBa_2Cu_3O_x$ film) was placed under an estimated pressure of $P \approx 4.5$ MPa while the thermal gradient was applied (in the low O_2 atmosphere). The temperature distribution across the sample was 290 °C – 395 °C. These conditions of applied pressure and the higher temperature value are very similar to what is reported in Ref. [29] for the de-twinning of $YBa_2Cu_3O_x$ single crystals. With the pressure along the length of the sample, then the preferential orientation is for the a axis to align with the pressure/thermal gradient, which necessarily means the (b-axis) Cu-O chains are aligned along the perpendicular direction. The a axis is then compressed and the b axis is dilated [43,44]. Oxygen diffuses most readily along the b axis, with the a-axis and c-axis diffusion rates approximately 10^2 and 10^6 times slower, respectively [45]. Such an orientation results in oxygen diffusion primarily along the width of the sample. It remains to be established as to why the $YBa_2Cu_3O_{\nabla x}$ film behaves as though it is untwinned after the removal of the applied pressure at the end of the process, although we suggest here a likely mechanism.

Taking into consideration the known intrinsic ferroelastic properties of $YBa_2Cu_3O_x$ [46–49], we propose that an internal static electric field arising from the oxygen gradient (charge doping) aligned along the a axis, (perpendicular to the b-axis Cu−O chains), provides the physical mechanism responsible for the observed behavior of $\Delta T_c(p)$ and locks in the apparent un-twinned configuration. The corresponding static electric fields within the three regions are approximately 37 V/m, 3.7 V/m, and 45 V/m, respectively, and 0.4–90 kV/m at the boundaries (see Appendix D). Then, taking into consideration results and conclusions from earlier independent studies, along with results here, it becomes conceivable that even the relatively low static electric fields arising from the charge doping gradient are sufficient to impact the structural stability of the lattice. Specifically, we note the following:

(1a) The observation of the correlation of static displacements between apical oxygen and planar copper atoms and the link between the chain and plane structures provided by the apical oxygen, which, as Etheridge observes [48], is such that "a local distortion in the chain could couple to a copper atom in the adjacent plane a coherence length away from it via the apical oxygen," along with evidence for the existence of electric dipole moments arising from the charge transfer from the Cu-O chains to the CuO_2 planes via the apical O(4) oxygen [50,51,58] (which together imply a correlation of dipoles two unit cells apart). Doping dependent dipole moments are formed in the CuO_2 plane at the O(1) and O(5) sites with $|p| \approx 0.002$ eÅ and 0.06 eÅ at O ≈ 6.5 and $|p| \approx 0.002$ eÅ and 0.015 eÅ at O ≈ 6.75. The primary component is along the c axis, however, there exist nonzero components in the a-b plane [50].

(1b) An upper estimate [47] of the twin domain wall energy of $E_D \approx 40$ meV/m^2 along with the coordinated motion of oxygen between the O(1) and (normally vacant) O(5) sites necessary for the formation or motion of a domain wall under applied stress.

(2a) The locally perturbed charge density distribution of connected networks of oxygen-pyramidal planes and the resulting inversion symmetry lacking nanodomains in which ferroelectricity and ferromagnetism are possible [48], as well as other experimental results consistent with ferroelectric behavior [47,52–54].

(2b) The intrinsic instabilities within the lattice, and the percolative nature of the superconducting path which is embedded in a poor metallic background [55–57].

(3a) The highly correlated nature of electronic charge doping in the CuO_2 plane and oxygen ordering in the Cu-O chains noted above in Refs. [18–20].

(3b) The apparent feedback mechanism between electronic doping and oxygen ordering observed here wherein the oxygen structures in the Cu-O chains (associated with the $p \approx 1/7$ and 1/8 doping states in the CuO_2 plane) are stabilized at temperatures (under the given oxygen pressure) at which they would not form under conventional conditions.

Taken together, the results noted above are consistent with a picture wherein the complexly coupled electronic and

structural order can be perturbed by a local static electric field. A comparison of the twin domain wall energy for a segment crossing a unit cell with that of the O(1) or O(5) dipole energy in the "charge-gradient" induced (a-b plane) electric field suggests that the motion of oxygen between the O(1) and O(5) sites is inhibited by this field. We estimate the unit cell domain wall energy as $E = E_D A \approx (40\ \mathrm{meV/m^2})(\sqrt{2}(3.86\ \text{Å})(11.4\ \text{Å})) \approx 2.5 \times 10^{-20}$ eV. Estimating an a-axis dipole moment of $|p| \approx 0.0001$ eÅ and then using $|E| = 37$ V/m gives $U_D = |p||E| \approx 3.7 \times 10^{-14}$ eV. While this comparison suggests that the electric field may be responsible for maintaining an untwinned film it is not readily apparent whether it is sufficient to produce (or retain) the strain necessary to result in the observed suppressed values of T_c. However, the potential existence of *nanoscale* ferroelasticity and ferroelectricity along with lattice instabilities would lend to such behavior. Alternatively, the interaction of the dipole moments with a large (applied) local electric field ($\sim$0.1 V/Å) is expected theoretically to impact the charge transfer mechanism between the Cu-O chains and the CuO_2 planes via oxygen reordering [50,51], which in turn would have an effect on the value of T_c. The magnitude of the electric field which we have estimated, however, is significantly less. Another consideration is the results from *ab initio* calculations which show the formation of in-plane strain induced surface dipoles due to charge redistribution within the CuO_2 planes from the Cu(2) to the O(2) and O(3) sites wherein compression (expansion) of the a axis (b axis) subtracts from the preexisting strong ionic dipole in the CuO_2 plane [22,23]. The interaction of the in-plane static electric field could potentially alter the Madelung potential between the apical O(4) and planar O(2)/O(3) sites resulting in a change of T_c [22,29]. Further along these lines, it is well known that the distance d_A of the apical oxygen to the planar copper atom in the CuO_5 pyramid varies more than any bond length in the cuprate family. As mentioned above, it has been shown that the length of d_A appears to determine the energy levels of electronic orbitals within this structure impacting the pairing interaction and subsequently the value of T_c [29–32]. Recent work involving similar layered complex oxides have shown how internal electrostatic fields can produce very large bond strains, subsequently altering dramatically the materials electronic properties [33–35].

An alternate explanation for the observed behavior not invoking a local electric field may well exist. The abrupt strain at the boundaries of the $p \approx 1/7$ plateau almost certainly has an effect on T_c in those regions, though as noted above, c-axis strain alone can only account for a small portion of the observed shifts in T_c. Future studies are planned to systematically investigate this, to address the issue of whether the film is in fact untwinned, as well as other related questions.

IV. CONCLUSIONS

The results presented here demonstrate a realizable approach to producing films of $YBa_2Cu_3O_x$ having varied doping levels on the same chip. In the course of establishing this novel sample preparation route, we have also observed that the $YBa_2Cu_3O_{\nabla x}$ film exhibits twin-free properties, i.e., behavior comparable to that observed for twin-free $YBa_2Cu_3O_x$ single crystals under uniaxial stress. We have also found new evidence furthering the already well-established link between oxygen, electronic, and structural ordering [18–20,48,56,57] in the form of local oxygen content stabilization against the annealing thermal gradient at the $p \approx 1/7$ level, and to a lesser extent at the $p \approx 1/8$ level as well.

We believe that the evolving electronic and structural nature of the $YBa_2Cu_3O_x$ films make them ideal for carrying out new experiments which could potentially discriminate between the many competing microscopic theories of superconductivity in the high-temperature cuprates as well as other compounds.

ACKNOWLEDGMENTS

This work was supported and funded by the Space and Naval Warfare Systems Center Pacific (SSC PAC) Naval Innovative Science and Engineering (NISE) Program and also by the U.S. Department of Energy (U.S. DOE), Office of Basic Energy Sciences, Division of Materials Sciences and Engineering under Grant No. DE-FG02-04-ER46105.

APPENDIX A: INTERPRETATION OF $T \gtrsim 85$ K MAGNETIZATION DATA

Due to the double valued nature of $T_c(p)$ at temperatures above $T \sim 85$ K, features in the $M(T)$ data (in Fig. 3) above this value can arise from both underdoped and overdoped

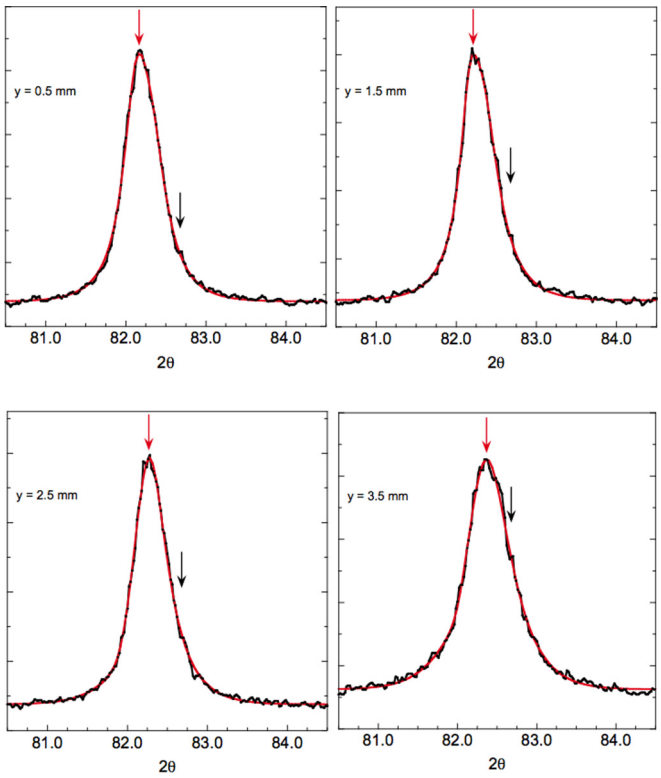

FIG. 11. (Color online) X-ray diffraction data for the $YBa_2Cu_3O_{\nabla x}$ film. Fits to the ⟨00 10⟩ peak for $y = 0.5$–3.5 mm. The red arrow indicates the maximum of the curve fit. The black arrow indicates a spurious substrate peak (which does not undergo change in 2θ as the oxygen content of the $YBa_2Cu_3O_{\nabla x}$ film does).

behavior. A small kink in the $M(T)$ data and center position data at $T \approx 86$ K and $T \approx 87$ K, respectively, can be correlated with the upper edge of the suppressed region of superconductivity ($p \approx 0.15$) observed in Ref. [9]. However, this temperature also correlates with the (extrapolated) critical temperature of the highest overdoped region of the film where $p \approx 0.195$ [see Fig. 7(c)]. To distinguish between the two we examine the magnetic moment center data in Fig. 3(b) where, at temperatures 87.5 K $\leqslant T \leqslant$ 90 K, the center position holds constant. This behavior would be consistent with a symmetrically weighted contribution to the magnetic response about the position having the maximum T_c value. Then, as both overdoped and underdoped portions of the film having the same T_c become superconducting, the center position of the measured magnetic moment would hold constant. Finally, when there is no more overdoped material left to become superconducting, the center of the signal will be pulled towards the underdoped side.

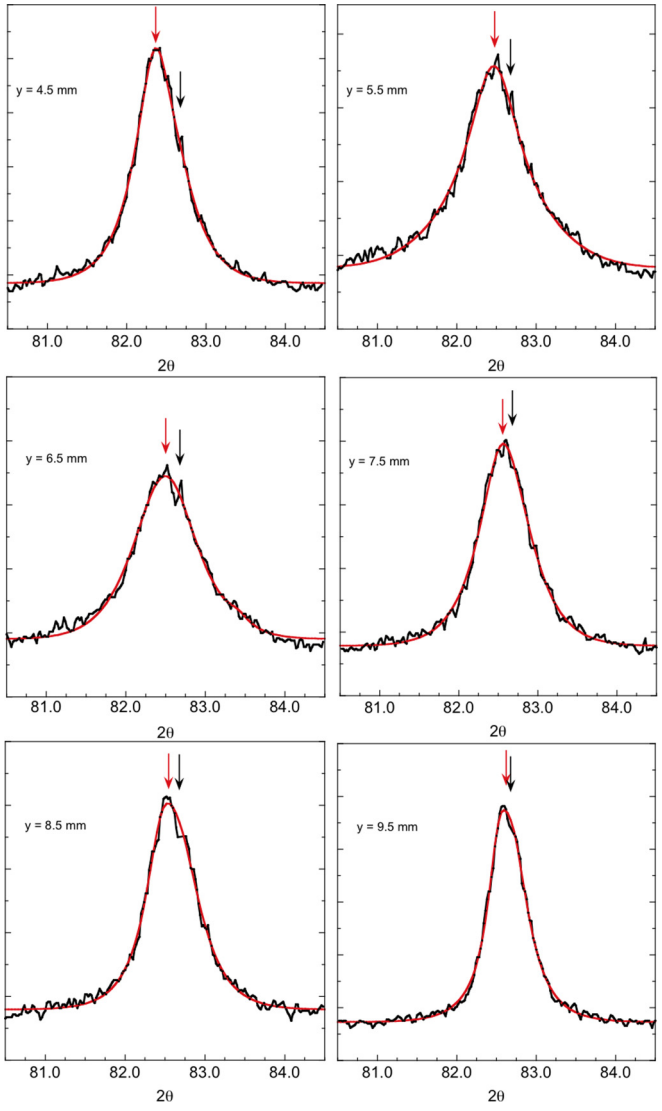

FIG. 12. (Color online) X-ray diffraction data for the $YBa_2Cu_3O_{\nabla x}$ film. Fits to the ⟨00 10⟩ peak for $y = 4.5$–9.5 mm. The red arrow indicates the maximum of the curve fit. The black arrow indicates a spurious substrate peak (which does not undergo change in 2θ as the oxygen content of the $YBa_2Cu_3O_{\nabla x}$ film does).

APPENDIX B: $\theta - 2\theta$ X-RAY DATA USED TO DETERMINE THE *c*-AXIS LENGTH

In Figs. 11 and 12 x-ray diffraction data (along with fits to the data) from the ⟨00 10⟩ peak are shown for the $YBa_2Cu_3O_{\nabla x}$ film sample. From the 2θ values, the lengths of the *c*-axis lattice parameter along the sample are calculated. The $\theta - 2\theta$ data is extracted from an integration of the data acquired using the Bruker D8 DISCOVER 2D detector. The x-ray scans are taken in three segments: from $14 < 2\theta < 40$, $35 < 2\theta < 70$, and $57 < 2\theta < 91$. Scans of the sample were taken such that the $\theta - 2\theta$ segment was held the same and the position, y(mm), along the sample was scanned in 1-mm increments. For the subsequent scan sequence(s) the scan position was returned to the initial point and the next $\theta - 2\theta$ scan was repeated at the same positions on the sample. From an examination of the observed 2θ position to the known values of the ⟨001⟩ and ⟨003⟩ peaks of the $SrTiO_3$ substrate, a small misalignment of the sample was found. Subsequently, a correction was made to the 2θ values of the ⟨004⟩ and ⟨00 10⟩ peaks used to calculate the *c*-axis lengths shown in Fig. 5(a) of the main text. The 2θ correction values used for each set of peaks are $\delta 2\theta = -.0578$, and $\delta 2\theta = 0.0039$, respectively.

APPENDIX C: SUPERCONDUCTING CRITICAL TEMPERATURE: RESISTIVE TRANSITION T_c VS *c*-AXIS LENGTH

Since the T_c vs y(mm) data on each of the two sets shown in Fig. 13 do not align exactly with respect to position on the sample, y(mm), polynomial curves were fit to various sections

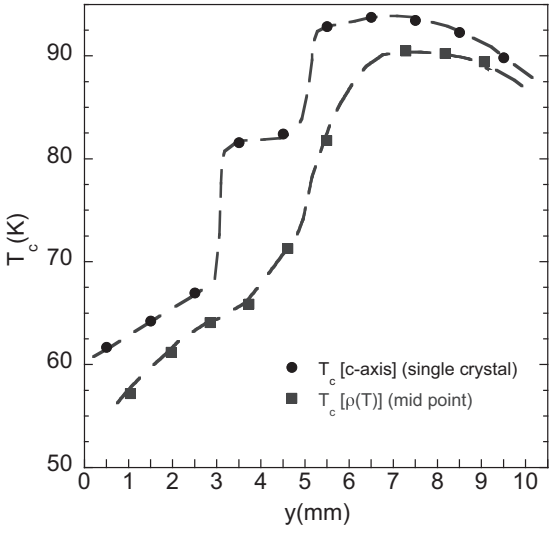

FIG. 13. Superconducting critical temperature vs sample position, T_c vs y(mm). Values of $T_c$were determined by the midpoint of the resistive transition (squares), and calculated from the *c*-axis lattice length extracted from x-ray diffraction data (circles) via the $T_c - c$(nm) relationship shown in Fig. (1 b) of Ref. [9]. Note that the maximum value of T_c for our sample is ≈3 K lower than that of their single crystals.

of each set of data. For clarity, continuous smoothed curves which follow the fitting to the various segments are shown as a guide to the eye. From the data and the subsequent curve fits shown, 19 values of ΔT_c are calculated. These values are displayed in Figs. 7(c) and 10 in the main text.

APPENDIX D: ESTIMATION OF THE CHARGE DOPING GRADIENT INDUCED ELECTRIC FIELD

We approach the scenario of the charge doping gradient along the a-axis direction as that of a simple capacitor, wherein the unit cell defines the volume and the two plates are parallel to the b axis with four Cu atoms on each plate. Then, the voltage drop across the two sides of the unit cell is given by $V = Qd/\epsilon A$, where the charge $Q = 4 \times (\Delta p/\Delta y) \times$ d is the *difference* in the charge doping level across the unit cell, $d = a = 3.823$ Å (the cell dimension along the a axis), $A = bc = (3.885$ Å$)(11.7$ Å$)$ is the area defined by the unit cell dimensions in the b- and c-axis directions, and $\epsilon \approx 6\epsilon_0$ [58]. As indicated in Fig. 7(c), the change in hole doping p, along the length of the sample y(mm) is $\Delta p/\Delta y \approx (6.1, 0.74, 7.4) \times 10^{-3}$ [(h/Cu)/(mm)] for the intervals $y =$ (0–2.8 mm), (3.45–4.65 mm), and (5.49–10 mm), respectively. Absent further data on how sharp the transition between these regions is, a lower limit of $\Delta p/\Delta y \approx 2.2 \times 10^{-2}$ [(h/Cu)/(mm)] is estimated. A very sharp transition of the order of a micron [see blue dashed lines in Fig. 7(c)] would give $\Delta p/\Delta y \approx 0.012 - 0.017$ [(h/Cu)/(μm)]. From this we find $E = V/a$ within the three regions is approximately 37 V/m, 3.7 V/m, and 45 V/m, respectively, and 0.4–90 kV/m at the boundaries.

[1] Y. Ando and K. Segawa, Phys. Rev. Lett. **88**, 167005 (2002).
[2] Y. Zuev, M. S. Kim, and T. R. Lemberger, Phys. Rev. Lett. **95**, 137002 (2005).
[3] J. E. Sonier, S. A. Sabok-Sayr, F. D. Callaghan, C. V. Kaiser, V. Pacradouni, J. H. Brewer, S. L. Stubbs, W. N. Hardy, D. A. Bonn, R. Liang, and W. A. Atkinson, Phys. Rev. B **76**, 134518 (2007).
[4] J. Singleton, Clarina de la Cruz, R. D. McDonald, S. Li, M. Altarawneh, P. Goddard, I. Franke, D. Rickel, C. H. Mielke, X. Yao, and P. Dai, Phys. Rev. Lett. **104**, 086403 (2010).
[5] B. J. Taylor, R. E. Baumbach, D. J. Scanderbeg, and M. B. Maple, Phys. Rev. B **81**, 174511 (2010).
[6] S. E. Sebastian, N. Harrison, and G. G. Lonzarich, Rep. Prog. Phys. **75**, 102501 (2012).
[7] X. G. Zheng, M. Suzuki, C. Xu, H. Kuriyaki, and K. Hirakawa, Physica C **271**, 272 (1996).
[8] H. Shaked, J. D. Jorgensen, J. Faber, Jr., D. G. Hinks, and B. Dabrowski, Phys. Rev. B **39**, 7363(R) (1989).
[9] R. Liang, D. A. Bonn, and W. N. Hardy, Phys. Rev. B **73**, 180505(R) (2006).
[10] T. B. Lindemer, J. F. Hunley, J. E. Gates, A. L. Sutton, Jr., J. Brynestad, C. R. Hubbard, and P. K. Gallagher, J. Am. Ceram. Soc. **72**, 1775 (1989).
[11] R. P. Vasquez, B. D. Hunt, and M. C. Foote, Appl. Phys. Lett. **53**, 2692 (1988).
[12] M. Gurvitch, J. M. Valles, Jr., A. M. Cucolo, R. C. Dynes, J. P. Garno, L. F. Schneemeyer, and J. V. Waszczak, Phys. Rev. Lett. **63**, 1008 (1989).
[13] W. H. Fietz, K. Grube, S. I. Schlachter, H. A. Ludwig, U. Tutsch, H. Wühl, K.-P. Weiss, H. Leibrock, R. Hauff, Th. Wolf, B. Obst, P. Schweiss, and M. Kläser, Physica C **341-348**, 347 (2000).
[14] W. H. Fietz, K.-P. Weiss, and S. I. Schlachter, Supercond. Sci. Technol. **18**, S332 (2005).
[15] C. C. Almasan, S. H. Han, B. W. Lee, L. M. Paulius, M. B. Maple, B. W. Veal, J. W. Downey, A. P. Paulikas, Z. Fisk, and J. E. Schirber, Phys. Rev. Lett. **69**, 680 (1992).
[16] S. W. Tozer, J. L. Koston, and E. M. McCarron III, Phys. Rev. B **47**, 8089 (1993).
[17] S. Sadewasser, J. S. Schilling, and A. M. Hermann, Phys. Rev. B **62**, 9155 (2000).
[18] D. de Fontaine, G. Cedar, and M. Asta, Nature (London) **343**, 544 (1990).
[19] R. McCormack, D. de Fontaine, and G. Ceder, Phys. Rev. B **45**, 12976 (1992).
[20] D. de Fontaine, V. Ozolins, Z. Islam, and S. C. Moss, Phys. Rev. B **71**, 212504 (2005).
[21] U. Welp, M. Grimsditch, S. Fleshier, W. Nessler, B. Veal, and G. W. Crabtree, J. Supercond. **7**, 159 (1994).
[22] W. E. Pickett, Phys. Rev. Lett. **78**, 1960 (1997).
[23] W. E. Pickett, Physica C **289**, 51 (1997).
[24] J. S. Schilling and S. Klotz, in *Physical Properties of High Temperature Superconductors*, Vol. III, edited by D. M. Ginsberg (World Scientific, Singapore, 1992).
[25] M. B. Maple, L. M. Paulius, and J. J. Neumeier, Physica C **195**, 64 (1992).
[26] J. L. Tallon, C. Bernhard, H. Shaked, R. L. Hitterman, and J. D. Jorgensen, Phys. Rev. B **51**, 12911(R) (1995).
[27] C. Meingast, T. Wolf, M. Kläiser, and G. Müller-Vogt, J. Low Temp. Phys. **105**, 1391 (1996).
[28] M. M. Milić, J. Phys. Chem. Solids **73**, 99 (2012).
[29] Y. Ohta, T. Tohyama, and S. Maekawa, Phys. Rev. B **43**, 2968 (1991).
[30] A. A. R. Fernandes, J. Santamaria, S. L. Bud'ko, O. Nakamura, J. Guimpel, and I. K. Schuller, Phys. Rev. B **44**, 7601 (1991).
[31] J. A. Slezak, J. Lee, M. Wang, K. McElroy, K. Fujita, B. M. Andersen, P. J. Hirschfeld, H. Eisaki, S. Uchida, and J. C. Davis, PNAS **105**, 3203 (2008).
[32] H. Zhoua, Y. Yacobyb, V. Y. Butkoa, G. Logvenova, I. Božović, and R. Pindak, PNAS **107**, 8103 (2010).
[33] V. Y. Butko, G. Logvenov, N. Božović, Z. Radović, and I. Božović, Adv. Mater. **21**, 3644 (2009).
[34] P. V. Balachandran, A. Cammarata, B. B. Nelson-Cheeseman, A. Bhattacharya, and J. M. Rondinelli, APL Materials **2**, 076110 (2014).
[35] B. B. Nelson-Cheeseman, H. Zhou, P. V. Balachandran, G. Fabbris, J. Hoffman, D. Haskel, J. M. Rondinelli, and A. Bhattacharya, Adv. Funct. Mater. **24**, 6884 (2014).
[36] U. Welp, M. Grimsditch, S. Fleshler, W. Nessler, J. Downey, G. W. Crabtree, and J. Guimpel, Phys. Rev. Lett. **69**, 2130 (1992).

[37] The data in Fig. 4(a) of Ref. [9] were fit to the following equation: $6 + x = 6.2623 - 1.601p + 63.409p^2 - 182.59p^3$ over the range $6.25 < 6 + x < 7$.
[38] C. L. Johnson, J. K. Bording, and Y. Zhu, Phys. Rev. B **78**, 014517 (2008).
[39] F. Krieth and M. S. Bohn, *Principles of Heat Transfer* (PWS Publishing, Boston, 1997).
[40] L. X. Cao, J. Zegenhagen, E. Sozontov, and M. Cardona, Physica C **337**, 24 (2000).
[41] H. Y. Zhai and W. K. Chu, Appl. Phys. Lett. **76**, 3469 (2000).
[42] M. Salluzzo, C. Aruta, G. Ausanio, A. D'Agostino, and U. S. di Uccio, Phys. Rev. B **66**, 184518 (2002).
[43] U. Welp, M. Grimsditch, H. You, W. K. Kwok, M. M. Fang, G. W. Crabtree, and J. Z. Liu, Physica C **161**, 1 (1989).
[44] D. L. Kaiser, F. W. Gayle, R. S. Roth, and L. J. Swartzendruber, J. Mater. Res. **4**, 745 (1989).
[45] S. J. Rothman, J. L. Routbort, U. Welp, and J. E. Baker, Phys. Rev. B **44**, 2326 (1991).
[46] H. Schmid, E. Burkhardt, B. N. Sun, and J.-P. Rivera, Physica C **157**, 555 (1989).
[47] J. R. LaGraff and D. A. Payne, Ferroelectrics **130**, 87 (1992).
[48] J. Etheridge, Phil. Mag. A **73**, 643 (1996).
[49] J. A. Jung and M. Abdelhadi, Proc. SPIE **4811**, 78 (2002).
[50] N. Chandrasekhar, O. T. Valls, and A. M. Goldman, Phys. Rev. B **49**, 6220 (1994).
[51] G. Grigelionis, E. E. Tornau, and A. Rosengren, Phys. Rev. B **53**, 425 (1996).
[52] L. R. Testardi, W. G. Moulton, H. Mathias, H. K. Ng, and C. M. Rey, Phys. Rev. B **37**, 2324(R) (1988).
[53] V. Müller, C. Hucho, K. de Groot, D. Winau, D. Maurer, and K. H. Rieder, Solid State Commun. **72**, 997 (1989).
[54] C. Hucho, D. Maurer, and V. Müller, J. Alloy. and Comp. **211-212**, 309 (1994).
[55] J. C. Phillips, Phys. Rev. Lett. **88**, 216401 (2002).
[56] J. C. Phillips, PNAS **105**, 9917 (2008).
[57] J. C. Phillips, J. Supercond. Nov. Magn. **23**, 1267 (2010).
[58] R. C. Baetzold, Phys. Rev. B **38**, 11304 (1988).